Scientific Reports

https://doi.org/10.1038/s41598-026-37878-0

Article in Press

Cordyceps sinensis enhances the efficacy of anti-PD-1 immunotherapy in Lewis lung adenocarcinoma

Received: 5 October 2025

Accepted: 27 January 2026

Published online: 04 February 2026

Cite this article as: Liu Y., Gao Y., Suonanlamao *et al. Cordyceps sinensis* enhances the efficacy of anti-PD-1 immunotherapy in Lewis lung adenocarcinoma. *Sci Rep* (2026). https://doi.org/10.1038/s41598-026-37878-0

Yingying Liu, Yaqi Gao, Suonanlamao, Yuanan Ma, Yuancan Xiao, Lixin Wei & Wenbin Zhou

Cordyceps sinensis enhances the efficacy of anti-PD-1 immunotherapy in Lewis lung adenocarcinoma

Yingying Liu[1,2,3], Yaqi Gao[1,2,3], Suonanlamao[4], Yuanan Ma[1,2,3], Yuancan Xiao[1,2], Lixin Wei[1,2*], Wenbin Zhou[1,2*]

***Co-corresponding author:**

Professor Lixin Wei

Qinghai Provincial Key Laboratory of Tibetan Medicine Pharmacology and Safety Evaluation, CAS Key Laboratory of Tibetan Medicine Research, Northwest Institute of Plateau Biology, Chinese Academy of Science, Xining, Qinghai, 810008, China

Email addresses: lxwei@nwipb.cas.cn

Dr. Wenbin Zhou

Qinghai Provincial Key Laboratory of Tibetan Medicine Pharmacology and Safety Evaluation, CAS Key Laboratory of Tibetan Medicine Research，Northwest Institute of Plateau Biology, Chinese Academy of Science, Xining, 810008.

Email: zhouwenbin@nwipb.cas.cn

Abstract

Background: Lung cancer, primarily non-small cell lung cancer (NSCLC), causes the highest cancer-related mortality. Although PD-1/PD-L1 inhibitors have improved survival in advanced NSCLC, they can cause immune-related adverse events. *Cordyceps sinensis* (*C. sinensis*), a traditional Chinese medicine used for tonifying the lung and kidney and enhancing immune function, has shown therapeutic promise in combination with anti-PD-1 therapy for NSCLC. This study aimed to explore the anti-tumor effect of wild *C. sinensis* combined with anti-mouse PD-1 in the treatment of Lewis lung adenocarcinoma (LLC) and to elucidate the underlying pharmacodynamic mechanism. **Methods:** LLC mouse model was established via inoculation with LLC cells, followed by treatment with anti-mouse PD-1, *C. sinensis*, or their combination. The tumor volume, weight, and histological changes of LLC mice were evaluated. The proportions of tumor-infiltrating immune cells in blood and tumors were evaluated by flow cytometry, immunohistochemistry, and immunofluorescence. The underlying mechanisms of the combination of *C. sinensis* and anti-mouse PD-1 therapy in LLC mice were investigated using an integrated transcriptomics and metabolomics analysis. **Results:** Treatment with anti-mouse PD-1, *C. sinensis*, or their combination significantly reduced tumor volume and weight, and attenuated the

histopathological changes of LLC mice tumors. Among which, medium-dose *C. sinensis* combination exhibited significant improvements. Furthermore, the combination of *C. sinensis* and anti-mouse PD-1 significantly increased the proportion of $CD8^+$ T cells and decreased the abundance of Tregs and PMN-MDSCs. Integrated transcriptomics and metabolomics analysis revealed that the combination of *C. sinensis* and anti-mouse PD-1 can enhance anti-tumor immunity in LLC mice by acting on key immune-related genes, including DGKA, PLA2G7, AMPD1, ATP8B4, and BST1, thereby modulating glycerophospholipid metabolism, the TCA cycle, purine metabolism, and nicotinate-nicotinamide metabolism. **Conclusions:** Wild *C. sinensis* combined with anti-mouse PD-1 therapy exerts therapeutic effects against LLC by targeting immune-related genes, modulating associated pathways, increasing the proportion of $CD8^+$ T cells, and reducing the infiltration of Tregs and PMN-MDSCs, thereby suppressing tumor growth and inhibiting LLC progression. Further research and clinical studies are needed to validate and expand upon these promising findings.

Keywords: *Cordyceps sinensis*, Anti-mouse PD-1, Lewis lung adenocarcinoma, Transcriptomics, Metabolomics, Anti-tumor effect

Introduction

Lung cancer (LC) is the most common and deadliest malignant tumor worldwide, posing a great threat to human health. Non-small-cell lung cancer (NSCLC) is the most prevalent type, accounting for approximately 80% of lung cancer cases [1]. Chemotherapy, radiotherapy, and molecular targeted therapy are the main clinical treatments for advanced LC. Although various chemotherapeutic agents and molecular-targeted agents have been administered in clinical practice, several challenges, such as limited efficacy and drug resistance to targeted therapy, lead to suboptimal therapeutic response. Given the very low 5-year survival rates among patients with advanced LC, there is an urgent need for new treatments and therapeutic agents in clinical practice [2].

Tumor immunotherapy technologies have developed rapidly in

recent years. Accumulated gene mutations in tumor cells can promote tumor growth and increase the chance of tumor cell recognition by immune cells. However, during tumor development and evolution, tumor cells can evade immune surveillance and maintain immunologic tolerance using immunosuppressive cytokines, chemokines, regulatory immune cells, and immune checkpoint signaling pathways to weaken the anti-tumor immune response [3]. With recent advancements in cancer immunotherapy, the regulation of anti-tumor immunity has received widespread attention and has become an important means of cancer treatment [4]. Immune checkpoint inhibitors (ICIs), such as programmed cell death 1/programmed cell death ligand 1 (PD-1/PD-L1) inhibitors, impede the interaction between PD-1 on immune cells and PD-L1 on tumor cells. This effect relieves T cell suppression, activates effector T cells, reverses immunosuppression in patients with cancer, and enables the immune system to identify and destroy tumor cells. PD-1 inhibitors, such as pembrolizumab (Keytruda), have been approved for treating various types of cancer, including lung cancer, malignant melanoma, and liver cancer. They have been shown to significantly improve tumor response rates and enhance patients' survival. Nevertheless, the clinical efficacy of PD-1 inhibitors is limited, and the response rate of single-agent use is between 10% and 40%. Moreover, PD-1 inhibitors are not effective against all tumor types. Only a proportion of patients with tumors sensitive to PD-1 inhibitors benefit from these drugs. In addition, accumulating

evidence has demonstrated that secondary resistance to PD-1 inhibitors occurs during cancer immunotherapy [5]. Thus, it is urgently needed to improve the clinical efficacy of PD-1 inhibitors, explore their mechanism of action, and overcome drug resistance.

Combining PD-1 inhibitors with traditional Chinese medicines (TCMs) for improving therapeutic efficacy has become a clinical focus. Several of these combination approaches have been successfully translated into clinical practice, yielding favorable outcomes in a portion of patients with cancer [6]. For example, Lv et al. [7] found that combined treatment with Gegen Qinlian decoction and anti-mouse PD-1 can significantly enhance the infiltration of $CD8^+$ T cells in tumor tissues and increase their proportion in peripheral blood. Kong et al. [8] reported that the Bushen Yiqi formula can inhibit tumor proliferation, promote apoptosis, and enhance the anti-tumor effects of anti-mouse PD-1 in Lewis lung adenocarcinoma (LLC) model mice. Li et al. [9] discovered that combined treatment with Qingrehuoxue formula and anti-mouse PD-1 can significantly enhance T-cell cytokine activity and lower the abundance of tumor-infiltrating M2 macrophages in NSCLC. Chen et al. [10] showed that Huaier exhibits synergistic effects with anti-mouse PD-1 therapy in colorectal cancer by activating MHC I and $CD8^+$ T cells, thereby overcoming microenvironmental immunosuppression. Collectively, previous studies have demonstrated that TCMs can improve the TME and enhance the efficacy of anti-mouse PD-1 therapy. These TCMs were typically

chosen for their long history of clinical use in anti-tumor applications or their well-established pharmacological properties, such as anti-inflammatory and antioxidant activities.

Wild *Cordyceps sinensis* (*C. sinensis*) possesses inherent immunomodulatory properties, which is the main reason for its traditional application, and also provides a rational basis for its utilization in the field of immuno-oncology [11]. *C. sinensis* consists of the fruiting body of the fungus in the Clavicipitaceae family and the dead larva of its parasitic host, *Hepialus armoricanus* (the Hepialidae family). According to the theory of TCM, *C. sinensis* is sweet in taste and neutral in nature, and it has the effects of tonifying the lung and kidney, stopping bleeding, and resolving phlegm. Recent clinical studies have shown that the Bailing capsule, whose main ingredient is fermented *C. sinensis* powder, can effectively improve fatigue, enhance the immune function, and prevent the complications of radiotherapy in patients with lung cancer [12-14]. A meta-analysis showed that fermented products or extracts of *C. sinensis*, when combined with conventional chemotherapy, can improve the immune function of patients with lung cancer by increasing the serum levels of IgA, IgG, IgM, CD4, CD8, and NK cells [15]. Lu et al. [16] indicated that the Bailing capsule exerted an anti-cancer effect against NSCLC mice by suppressing MAPK pathway-mediated tumor cell proliferation. The result also showed that, compared with the single therapy of *C. sinensis* or anti-mouse PD-1, their combination exerted better anti-tumor effect.

However, the subjects in previous studies were almost artificially cultured *C. sinensis* or *C. sinensis* preparations. Wild *C. sinensis*, which is distributed in the Qinghai-Tibet Plateau and surrounding areas at an altitude of 3200-5300 m. It potentially accumulates numerous substances or secondary metabolites with specific or therapeutic effects [17]. This unique attribute suggests that wild *C. sinensis* may possess special immunomodulatory properties. In this study, we observed the effect of the application of wild *C. sinensis* as well as its combination therapy with anti-mouse PD-1. The pharmacodynamic characteristics were evaluated and the mechanism underlying the combination of wild *C. sinensis* and anti-mouse PD-1 therapy on mice with LLC was investigated using a combination of transcriptomics, metabolomics, hematoxylin-eosin (H&E) staining, flow cytometry (FC), immunohistochemistry (IHC), and immunofluorescence (IF).

Materials and methods

Preparation of experimental drugs

Wild *C. sinensis*, obtained from the Yushu River source *Cordyceps sinensis* specialized cooperatives in Yushu, China, was powdered and dissolved in normal saline. The anti-mouse PD-1 mAb was purchased from Bioxcell (BE0146), and the liquid was dissolved in PBS. *C. sinensis* was administered by gavage in three dosages (462.5 mg/kg; 925 mg/kg; 1850 mg/kg) at a volume of 10 μL/g, 20μL/g, 20μL/g per day, respectively. The anti-mouse PD-1 mAb was administered via

intraperitoneal injection (10 mg/kg twice weekly) at a volume of 10 µL/g.

Experimental animals and cell line

LLC cells were obtained from Shanghai Southern Model Biotechnology Co., Ltd. (China). The culture medium comprised 90% RPMI-1640 (Gibco Life Technologies, Grand Island, USA), 10% FBS (Gibco Life Technologies, Grand Island, USA), and 1% double antibody (Gibco Life Technologies, Grand Island, USA). Ninety 6-week to 8-week-old female SPF C57BL/6 mice were purchased from Shanghai Southern Model Biotechnology Co., Ltd. (China). Following a 5-day acclimation under standard laboratory conditions (22 ± 2°C, 40%-70% humidity, and 12/12-h light/dark cycles), the mice were subjected to experimental procedures. The study protocol (allowance number NWIPB2023–19) was approved by the Animal Experimentation Committee of Northwest Plateau Biology Institute, Chinese Academy of Sciences. The animal experiments followed the ARRIVE guidelines (https://arriveguidelines.org), and all experiments were performed in accordance with the relevant guidelines and regulations.

Animal model

LLC cells in the logarithmic growth phase were collected and suspended in PBS at 5 × 10^6 cells/mL. A 0.1 mL aliquot was subcutaneously injected into the right flank of each mouse. A day

after inoculation, the living conditions of the mice were observed, before touching the inoculation site by hand to detect subcutaneous tumors. After eliminating mice with too large, too small, and irregularly shaped tumors and underweight mice, the mice were randomly divided into eight groups (average tumor volume: approximately 40-60 mm^3 in each group; n = 8 mice per group): the vehicle group (Vehicle); anti-mouse PD-1 mAb group (mPD-1, 10 mg/kg); low-dose *C. sinensis* group (L-CS, 462.5 mg/kg); medium-dose *C. sinensis* group (M-CS, 925 mg/kg); high-dose *C. sinensis* group (H-CS, 1850 mg/kg); low-dose *C. sinensis* combined with anti-mouse PD-1 group (462.5 mg/kg of *C. sinensis* + 10 mg/kg of mPD-1, L-CS + mPD-1); medium-dose *C. sinensis* combined with anti-mouse PD-1 group (925 mg/kg of *C. sinensis* + 10 mg/kg of mPD-1, M-CS + mPD-1); high-dose *C. sinensis* combined with anti-mouse PD-1 group (1850 mg/kg of *C. sinensis* + 10 mg/kg of mPD-1, H-CS + mPD-1). The administration protocol for all treatment groups was designed based on the preparation method of the experimental drugs. PBS was used as the treatment for mice in the Vehicle group. All animals received the corresponding intervention for 2 weeks, and the day of animal grouping was regarded as day 0 of the intervention.

In vivo anti-tumor experiment

After grouping and initiating the interventions, mouse weight was measured daily. Tumor volume was also recorded daily using the following formula: tumor volume (mm^3) = length (mm) × width

$(mm)^2 \times 0.5$. At the end of the study, all mice were sacrificed, and the excised tumors were subsequently weighed. The tumor growth inhibition rate (TGI) was calculated as follows: TGI (%) = [1-(tumor volume in the treatment group) / (tumor volume in the vehicle group)] × 100. Following collection, tumors were processed for various analyses. A portion was snap-frozen in liquid nitrogen for storage at -80°C, while another portion was fixed for H&E staining, IHC, and IF. Additionally, blood samples were collected for FC analysis.

H&E staining

Following fixation in 4% paraformaldehyde at room temperature for 24 h, the tumor tissue was embedded in paraffin and sectioned into 5-μm slices. Pathological evaluation was conducted on these sections after H&E staining, using light microscopy (Olympus Corporation, Tokyo, Japan) at 200× magnification.

FC analysis

Blood samples from the Vehicle, mPD-1, M-CS, and M-CS + mPD-1 groups were collected in tubes containing sodium heparin. Single-cell suspensions were subsequently prepared by lysing red blood cells. The cells were stained via incubation with fluorescently-labeled antibodies at 4°C for 30 min to identify live cells, $CD45^+$, $CD11b^+$, $CD3^+$, $CD8^+$, $CD4^+$, and $Foxp3^+$ cells. The samples were analyzed on a CytoFLEX flow cytometer, and the results were analyzed using the software FlowJo. The gating strategy of each cell

group is shown in Fig. S1.

IHC and IF staining

The paraffin specimens were dewaxed, antigens were repaired with citrate buffer (C1032; Solarbio, Beijing, China), and the specimens were incubated with rabbit anti-mouse CD45, rabbit anti-mouse CD3, rabbit anti-mouse CD8, rabbit anti-mouse CD4, and rabbit anti-mouse Foxp3 at 4°C overnight. The next day, the specimens were incubated with the HRP-labeled goat anti-rabbit IgG and streptavidin biotin complex. Thereafter, diaminobenzidine (DAB) staining, hematoxylin staining, and alcohol color separation were conducted, followed by xylene transparency and neutral gum sealing. The images were obtained via an optical microscope. In CD3, CD8, CD4, and Foxp3 staining, cells with brown particles were regarded as positive cells. Quantitative assessment was conducted by measuring the average integrated optical density of the positive staining area using Image-Pro Plus 6.0 software. For IF staining, tumor sections were deparaffinized, rehydrated, and subjected to antigen retrieval. The sections were then blocked with donkey serum, and the tissues were incubated with primary antibodies against Ly6G and CD11b at 4°C overnight. Following PBS rinses, the sections were dark incubated with fluorescent secondary antibodies at 37°C for 50 min. Cell nuclei were then counterstained with DAPI, after which the slides were mounted and images were captured. The fluorescence intensity was quantified using Image-Pro Plus 6.0 software.

Transcriptomics sequencing analysis

Trizol reagent (Invitrogen, CA, USA) was adopted to extract total RNA from the tumor tissue of mice in the Vehicle, mPD-1, M-CS, and M-CS + mPD-1 groups. RNA concentration and purity in the tumor tissues were determined using the NanoDrop 2000 spectrophotometer (Thermo Scientific, USA). RNA integrity was assessed using the Agilent 2100 Bioanalyzer (Agilent Technologies, Santa Clara, CA, USA). Sequencing was performed on an Illumina NovaSeq 6000 platform. Differentially expressed genes (DEGs) were screened based on the criteria of $P < 0.05$ and |Fold Change| > 2 or |Fold Change| < 0.5 to enhance the scientific validity of the sequencing results. Volcano and heatmap plots were generated using the "ggplot2" and "pheatmap" packages of R, respectively. Immune and matrix abundance were estimated using the "MCPcounter" package. The proportion of $CD8^+$ T cells, $CD4^+$ T cells and Tregs was analyzed using CIBERSORT. The GSEA software was employed to conduct gene set enrichment analysis using the "h.all. V2025.1.Hs.symbols.gmt" subset from the MSigDB. Enrichment scores (ES) were calculated based on 1,000 random permutations per category, and statistical significance was determined based on P values.

Metabolomics analysis

Tumor tissue from mice in the Vehicle, mPD-1, M-CS, and M-CS +

mPD-1 groups was collected for metabolomics analysis. Following lyophilization, the samples were homogenized and extracted in 1 mL of precooled methanol/acetonitrile/water (2:2:1, v/v) with ultrasonication on ice. Then, the extract was incubated at -20°C for 1 h and centrifuged at 14,000 g at 4°C for 20 min. The resulting supernatant was vacuum-dried and reconstituted in 50% acetonitrile. A quality control (QC) sample was formed by mixing equal volumes of each sample. After filtration through a 0.22 μm membrane, the samples were transferred to HPLC vials before analysis. LC-MS/MS analysis and data processing were conducted following previously described methods [18].

Integrated transcriptomics and metabolomics analysis

An integrative analysis was conducted through a sequential process. First, a signature gene set for immune cells was defined by taking the intersection between the CIBERSORT LM22 gene set and our transcriptomics data. Subsequently, differential metabolites were imported into Cytoscape (Version 3.10.3), using the MetScape plugin to generate a metabolic network. Finally, the immune cell signature gene set was mapped onto this network, constructing a compound-reaction-enzyme-gene network that establishes direct functional links between immune gene expression and altered metabolic pathways.

Statistical analysis

Statistical analysis was conducted using SPSS 19.0 software. Data were analyzed using one-way analysis of variance (ANOVA) followed by the *post hoc* Bonferroni test, with $P < 0.05$ considered statistically significant. All data are expressed as mean ± standard deviation (SD).

Results

The combination of *C. sinensis* and anti-mouse PD-1 exhibited a significant inhibitory effect on the growth of LLC tumors

Compared to the Vehicle group, none of the treatment groups affected the body weight change of mice following a 13-day treatment ($P > 0.05$) (Fig. 1A). On the 13th day, all treatment groups exhibited a significant reduction in tumor volume compared to the Vehicle group ($P < 0.05$, $P < 0.01$) (Fig. 1B). Among them, the L-CS + mPD-1, M-CS + mPD-1, and H-CS + mPD-1 groups showed a significant decrease in tumor volume compared to the mPD-1 group ($P < 0.01$). The M-CS + mPD-1 group showed a significant decrease in tumor volume compared to the M-CS group ($P < 0.05$). We calculated the TGI rates to quantify the anti-tumor efficacy. The TGI for the mPD-1, L-CS, M-CS, H-CS, L-CS + mPD-1, M-CS + mPD-1, and H-CS + mPD-1 groups was 14.96%, 33.28%, 34.57%, 48.03%, 39.20%, 51.24%, and 51.24%, respectively. Compared to the Vehicle group, the tumor weights were significantly decreased in all treatment groups ($P < 0.05$, $P < 0.01$) (Fig. 1C), indicating that the combined treatment of *C. sinensis* and anti-mouse PD-1 effectively

inhibited tumor growth in LLC mice.

The combination of *C. sinensis* and anti-mouse PD-1 ameliorated the histopathological changes of LLC tumors

The results of H&E staining are shown in Figs. 1D-K. In the Vehicle group, the tumor tissue exhibited varying sizes of tumor cells, significant cellular pleomorphism and atypia. The tumor cells displayed a round or oval morphology, accompanied by numerous mitotic figures, patchy necrosis and extensive hemorrhage. The demarcation of the tumor tissue is indistinct, with a limited infiltration of inflammatory cells within the surrounding connective tissue. All treatment groups alleviated the phenomena of tumor cell necrosis, interstitial hemorrhage, and inflammatory cell infiltration to varying degrees. Among them, the M-CS + mPD-1 group exhibited fewer mitotic figures, no evident necrosis, no apparent stromal hemorrhage, and no discernible infiltration of inflammatory cells.

The combination of *C. sinensis* and anti-mouse PD-1 increased the abundance of $CD8^+$ T cells and decreased the abundance of Tregs in blood

FC analysis revealed no significant differences in the percentage of $CD45^+$ immune cells among the mPD-1, M-CS, M-CS + mPD-1, and Vehicle groups (Figs. 2A and E). The proportion of $CD3^+$ T cells was significantly increased in the mPD-1, M-CS, and M-CS + mPD-1 groups compared to the Vehicle group ($P < 0.05$, $P < 0.01$).

Moreover, the M-CS + mPD-1 group exhibited a significant increase in the proportion of $CD3^+$ T cells relative to the M-CS group ($P < 0.01$) (Figs. 2B and E). Compared to the Vehicle group, the proportion of $CD8^+$ T cells was significantly increased in the mPD-1 and M-CS + mPD-1 groups ($P < 0.05$). Additionally, the M-CS + mPD-1 group showed a significant increase in $CD8^+$ T cells proportion compared to the M-CS group ($P < 0.05$) (Figs. 2C and E). The proportion of $CD4^+$ T cells did not significantly change among the four groups (Figs. 2C and E). The combined treatment of *C. sinensis* and anti-mouse PD-1 significantly reduced the proportion of $Foxp3^+$ Tregs compared to the Vehicle group and the mPD-1 group ($P < 0.01$) (Figs. 2D and E).

The combination of *C. sinensis* and anti-mouse PD-1 enhanced $CD8^+$ T cell infiltration and inhibited Treg and PMN-MDSC in the tumor tissues

IHC assay showed that the proportion of $CD3^+$ T cells was significantly increased in the mPD-1 and M-CS + mPD-1 groups compared to the Vehicle group ($P < 0.01$). Additionally, the M-CS + mPD-1 group showed a significant increase in $CD3^+$ T cells proportion compared to the mPD-1 group and the M-CS group ($P < 0.01$) (Figs. 3A and F). The proportion of $CD8^+$ T cells was significantly increased in the mPD-1 group compared to the Vehicle group ($P < 0.05$). Furthermore, the M-CS + mPD-1 group exhibited a significant decrease in the proportion of $CD8^+$ T cells relative to

the mPD-1 group ($P < 0.05$) (Figs. 3B and F). The proportion of $CD4^+$ T cells exhibited no significant difference between the groups (Figs. 3C and F). Compared to the Vehicle group, the proportion of $Foxp3^+$ Tregs was significantly decreased in the M-CS and M-CS + mPD-1 groups ($P < 0.01$), while the mPD-1 group showed no significant difference (Figs. 3D and F). IF assay revealed that the proportion of PMN-MDSCs (defined as $CD11b^+Ly6G^+$) was significantly decreased in the M-CS group compared to the Vehicle group ($P < 0.05$). A similar decreasing trend was observed in the M-CS + mPD-1 group, although it did not show statistical significance compared to the Vehicle group. The M-CS + mPD-1 group showed a significant decrease in the proportion of PMN-MDSCs relative to the mPD-1 group ($P < 0.01$) (Figs. 3E and F).

The combination of *C. sinensis* and anti-mouse PD-1 altered transcriptomic profiles and immune infiltration in LLC mice

Then, we conducted RNA sequencing on tumor tissues from mice in the Vehicle, mPD-1, M-CS, and M-CS + mPD-1 groups to explore the DEGs and immune cell infiltration. Compared to the Vehicle group, 348 genes were differentially expressed in the mPD-1 group ($P < 0.05$), including 181 downregulated and 167 upregulated DEGs; 317 genes were differentially expressed in the M-CS group ($P < 0.05$), including 198 downregulated and 119 upregulated DEGs; and 334 genes were differentially expressed in the M-CS + mPD-1 group ($P < 0.05$), including 219 downregulated and 115 upregulated DEGs

(Figs. 4A-C). The heatmap of DEGs is presented in Fig. 4G. KEGG analyses revealed enrichment of immune-related pathways, including IL-17 signaling pathway, Th1 and Th2 cell differentiation, Th17 cell differentiation, natural killer cell-mediated cytotoxicity and NOD-like receptor signaling pathway (Figs. 4D-F).

The MCP counter algorithm further indicated that treatment with mPD-1, M-CS, and M-CS + mPD-1 was associated with increased infiltration of T cells and endothelial cells. Treatment with M-CS + mPD-1 decreased the proportion of fibroblasts (Fig. 4H). Additionally, CIBERSORT analysis indicated that the mPD-1 group had a higher proportion of $CD8^+$ T cells ($P < 0.01$), while the M-CS and M-CS + mPD-1 groups exhibited a reduced Tregs fraction ($P < 0.05$) (Fig. 4I). GSEA analysis confirmed that genes associated with $CD8^+$ T cell activation and $CD4^+$ T cell activation were enriched in the M-CS + mPD-1 group (Figs. 4J and K). In contrast, genes associated with Treg cell activation were not enriched in the M-CS + mPD-1 group (Fig. 4L).

The combination of *C. sinensis* and anti-mouse PD-1 altered the metabolic profiles of tumors in LLC mice

Subsequently, we conducted a non-targeted metabolomics analysis on tumor tissues from the Vehicle, mPD-1, M-CS, and M-CS + mPD-1 groups. The PCA, PLS-DA and OPLS-DA score plots revealed significant differences between the samples of the four groups (Figs. 5A-C). OPLS-DA analysis was then conducted to compare mPD-1, M-

CS, and M-CS + mPD-1 with Vehicle to identify differential metabolites (Figs. 5D, G, and J). Permutation tests (n = 999) were performed to investigate the statistical significance of the OPLS-DA calibration. The blue R2 values and the red Q2 values (on the left) were consistently lower than those on the right (Figs. 5E, H, and K), demonstrating that the original model had valid predictive performance and high reliability. The differentially expressed metabolites were identified based on VIP > 1.0 and $P < 0.05$, and their results were depicted using volcano plots (Figs. 5F, I, and L).

The metabolic network was constructed using MetaboAnalyst 6.0 to investigate pathways affected by anti-mouse PD-1, *C. sinensis*, and their combination. Fig. 5M shows enriched pathways from the mPD-1 *vs.* Vehicle comparison, with purine metabolism and glycerophospholipid metabolism identified as significant. Fig. 5N shows the enriched pathways from the M-CS *vs*. Vehicle comparison, identifying glycerophospholipid metabolism, beta-alanine metabolism, and arginine and proline metabolism as the significant pathways. The M-CS + mPD-1 *vs.* Vehicle comparison revealed purine metabolism and glycerophospholipid metabolism as significant pathways (Fig. 5O).

The combination of *C. sinensis* and anti-mouse PD-1 exerted anti-tumor effects through a specific set of altered metabolites

To identify key metabolites underlying *C. sinensis*-enhanced anti-

tumor effects of anti-mouse PD-1 therapy, we performed a four-group Venn analysis. There were 124 specific metabolites in the M-CS + mPD-1 compared to the Vehicle group (Fig. 6A), which mainly affected glycerophospholipid metabolism, the TCA cycle, purine metabolism, and nicotinate and nicotinamide metabolism (Fig. 6B). Next, we explored how specific metabolites affect the response to anti-mouse PD-1 therapy. Supervised hierarchical clustering was conducted using the 20 metabolites, which were common in the M-CS + mPD-1 *vs.* Vehicle and the mPD-1 *vs.* Vehicle but absent in the M-CS *vs.* Vehicle (Fig. 6C). We focused on metabolites with higher abundance in the M-CS + mPD-1 group, including 1-hexadecyl-glycero-3-phosphate, 1-stearoylglycerophosphoserine, LPI(18:2), dihydrocorticosterone, 2-{3-[4-(tert-butyl)phenoxy]-4-oxochromen-7-yloxy}-N-(4-methylphenyl)acetamide, and LPE(P-16:0). We also focused on those with lower abundance, including Phe-Pro, PI(18:0/20:4) and 3-hydroxydodecanedioic acid (Fig. 6C). Notably, most of these differential metabolites are associated with glycerophospholipid metabolism.

The result of integrated transcriptomics and metabolomics analysis

The integrated approach identified seven key genes, including DGKA, PLA2G7, ACHE, AMPD1, ATP8B4, BST1, and CD38. The related metabolites included LPC, isocitrate, citrate, fumarate, ATP, ADP, and nicotinate. The affected pathways included glycosphingolipid

metabolism, the TCA cycle, purine metabolism, and nicotinate and nicotinamide metabolism (Fig. 7A). Then, we analyzed the expression levels of these seven key genes in the original transcriptomics data. Compared to the Vehicle group, the M-CS + mPD-1 group showed a significant decrease in the expression of DGKA, PLA2G7, ATP8B4, and BST1 ($P < 0.05$, $P < 0.01$), and a significant increase in the expression of AMPD1 ($P < 0.01$) (Fig. 7B).

Discussion

In this study, we established LLC mouse model and treated with anti-mouse PD-1, *C. sinensis*, or their combination. This provided a deeper insight into the mechanism by which *C. sinensis* enhances the therapeutic effect of anti-mouse PD-1 on LLC mice. Firstly, all treatment groups significantly reduced tumor volume and weight, and attenuated the histopathological changes of LLC tumors. Among which, medium-dose *C. sinensis* combination exhibited greater improvements. Then, the FC, IHC, and IF results showed that the M-CS + mPD-1 group significantly increased the proportion of $CD8^+$ T cells and decreased the abundance of Tregs and PMN-MDSCs. Based on these findings, RNA sequencing was conducted to determine if these effects were driven by alterations at the transcript level. Transcriptomics analysis indicated that the M-CS + mPD-1 group exhibited an increase in the expression of $CD8^+$ T cells-associated genes and a decrease in the expression of Tregs-associated genes.

Recent studies have shown that a higher abundance of T cells is

correlated with improved survival outcomes in various types of cancer, including lung cancer. A high abundance of $CD8^+$ T cells has been associated with more favorable prognostic outcomes in lung adenocarcinoma [19]. Additionally, $CD4^+$ T cells are phenotypically heterogeneous and can be classified into several T helper subsets. Among these subsets, Tregs play a critical role in suppressing immune activation, maintaining self-tolerance, and enhancing immunosuppression in the TME, thereby facilitating tumor immune evasion in lung cancer [20]. MDSCs constitute a heterogeneous population of immature myeloid cells that exhibit potent immunosuppressive activities through interactions with several types of immunocompetent cells. Our experimental results showed that the combination of *C. sinensis* and anti-mouse PD-1 significantly increased the proportion of $CD8^+$ T cells and decreased infiltration of immunosuppressive cells, including Tregs and PMN-MDSCs, then markedly suppressed tumor growth, and inhibited the progression of LLC.

Next, we conducted a non-targeted metabolomics analysis to determine whether the combination of *C. sinensis* and anti-mouse PD-1 altered the metabolic profiles of tumors in LLC mice. The analysis revealed a significantly altered tumor metabolic profile in the M-CS + mPD-1 group, with the differential metabolites primarily enriched in glycerophospholipid metabolism and purine metabolism. Additionally, we observed two key sets of metabolites underlying *C. sinensis*-enhanced anti-tumor effects of anti-mouse PD-1 therapy.

First, 124 specific metabolites were identified in the M-CS + mPD-1 compared to the Vehicle group, which mainly affected glycerophospholipid metabolism, the TCA cycle, purine metabolism, and nicotinate and nicotinamide metabolism. Second, 20 metabolites were regulated by the mPD-1 and M-CS + mPD-1 groups, but their abundance was significantly modulated in the M-CS + mPD-1 group. Most of these metabolites were involved in glycerophospholipid metabolism.

Then, we constructed a compound-reaction-enzyme-gene network using the immune-related genes and differential metabolites from the M-CS + mPD-1 group. The network analysis mapped the seven key genes and their related metabolites onto four core metabolic pathways: 1) Glycerophospholipid metabolism involved the DGKA, PLA2G7, and ACHE genes and the metabolite LPC. 2) The TCA cycle involved the PLA2G7 gene and isocitrate, citrate, and fumarate as metabolites. 3) Purine metabolism included the AMPD1 and ATP8B4 genes, and ATP and ADP as metabolites. 4) Nicotinate and nicotinamide metabolism involved the BST1 and CD38 genes and nicotinate as the metabolite. Compared to the Vehicle group, the M-CS + mPD-1 group exhibited significant downregulation of DGKA, PLA2G7, ATP8B4, and BST1 and upregulation of AMPD1.

DGKA, a key enzyme that phosphorylates diacylglycerol (DAG) into phosphatidic acid (PA) to regulate lipid metabolism, is highly expressed in NSCLC. Recent studies have reported that DGKA

inhibition can postpone T cell exhaustion, delay the resistance to PD-1 blockade, and enhance the efficacy of anti-PD-1 therapy in NSCLC [21]. PLA2G7, also known as lipoprotein-associated phospholipase A2, is highly expressed in hepatocellular carcinoma and bladder cancer, where it promotes immune escape [22, 23]. Pharmacological inhibition of PLA2G7 enhances the therapeutic efficacy of anti-PD-1 treatment in cancer models. However, its role in the TME of LLC remains poorly understood. Our findings may provide novel insights into potential therapeutic strategies for LLC immunotherapy. Importantly, as a key pathway regulated by DGKA and PLA2G7, glycerophospholipid metabolism has been identified as the most significantly affected lipid metabolism pathway across a spectrum of early-stage lung cancers [24]. Additionally, the dysregulated TCA cycle in tumors impairs $CD8^+$ T cells function, wherein elevated levels of its intermediates, succinate and fumarate, directly suppress anti-tumor activity [25]. In our study, the M-CS + mPD-1 group significantly decreased the expression of DGKA and PLA2G7, reduced isocitrate, citrate, and fumarate levels, and increased LPC levels, indicating that the combination therapy enhanced anti-tumor immunity by targeting DGKA and PLA2G7, thereby modulating glycerophospholipid metabolism and the TCA cycle to promote $CD8^+$ T cell infiltration and alleviate immunosuppression.

AMPD1, a key deaminase in purine metabolism, plays a significant role in regulating the tumor microenvironment and is positively correlated with the abundance of $CD4^+$ and $CD8^+$ T cells

[26]. In contrast, ATP8B4 encodes a protein that is a component of the P4-ATPase flippase complex. It is involved in purine metabolism and is negatively correlated with $CD8^+$ T cell infiltration [27]. Recent studies have shown that targeting purine metabolism can alleviate immunosuppressive function and enhance anti-tumor immunity in NSCLC [28]. In this study, the M-CS + mPD-1 group significantly increased the expression of AMPD1, decreased the expression of ATP8B4, and reduced ATP and ADP levels. These findings suggest that combination therapy may regulate the expression of key genes AMPD1 and ATP8B4 in purine metabolism to enhance $CD8^+$ T cell infiltration and mitigate immunosuppression.

BST1, also known as CD157, is a myeloid cell surface marker that functions as a β-NAD^+ metabolizing ectoenzyme. It contributes to the formation of an immunosuppressive TME that promotes tumor progression [29, 30]. Notably, BST1 drives the dysregulation of nicotinate and nicotinamide metabolism, increasing nicotinamide levels. Increased levels of nicotinamide have been shown to impair the differentiation and effector functions of $CD8^+$ T cells [31]. In the present study, the combination of *C. sinensis* and anti-mouse PD-1 reduced BST1 and nicotinate levels, enhancing anti-tumor immunity by targeting BST1-mediated nicotinate and nicotinamide metabolism and alleviating immunosuppression in the TME.

These results suggest that the combination of *C. sinensis* and anti-mouse PD-1 can enhance anti-tumor immunity in LLC mice by acting on key immune-related genes, including DGKA, PLA2G7,

AMPD1, ATP8B4, and BST1, thereby regulating several metabolic pathways, such as glycerophospholipid metabolism, the TCA cycle, purine metabolism, and nicotinate and nicotinamide metabolism. These metabolic alterations then enhanced the immune response in the TME, which was characterized by enhanced $CD8^+$ T cells infiltration, decreased abundance of Tregs and PMN-MDSCs (Fig. 8).

Nonetheless, this study had some limitations. First, the sample size of LLC tumor-bearing mouse models was small, and there might be some biases. Second, this project was mainly based on *in vivo* animal models, lacking supporting *in vitro* data. Moreover, the mechanism elucidated in this study should be verified using human samples. Additionally, the use of the herbal preparation *C. sinensis*, with its complex composition, poses the potential for off-target effects, and the specific active components responsible for the observed effect remain to be identified. Furthermore, the association between metabolism and immunity is preliminary and needs further functional validation.

Conclusion

Wild *C. sinensis* combined with anti-mouse PD-1 therapy exerted therapeutic effects against LLC by targeting key immune-related genes, including DGKA, PLA2G7, AMPD1, ATP8B4, and BST1, thereby modulating glycerophospholipid metabolism, the TCA cycle, purine metabolism, and nicotinate-nicotinamide metabolism. These metabolic changes enhanced the immune response in the TME, as

evidenced by a significant increased in the proportion of $CD8^+$ T cells and a decreased infiltration of immunosuppressive cells, including Tregs and PMN-MDSCs. Subsequently, this markedly suppressed tumor growth and inhibited the progression of LLC. Importantly, this study provides mechanistic insights into the therapeutic potential of *C. sinensis* in combination with anti-mouse PD-1 for the treatment of LLC, offering a promising strategy for future clinical applications.

Abbreviations

NSCLC	Non-small cell lung cancer
ICIs	Immune checkpoint inhibitors
PD-1	Programmed cell death-1
PD-L1	Programmed cell death ligand 1
C. sinensis	*Cordyceps sinensis*
DAB	Diaminobenzidine
DEGs	Differentially expressed genes
FC	Flow cytometry
LLC	Lewis lung adenocarcinoma
LC	Lung cancer
TCMs	Traditional Chinese medicines
TGI	Tumor growth inhibition rate
H&E	Hematoxylin-eosin
ES	Enrichment scores
QC	Quality control

OPLS-DA	Orthogonal partial least squares discriminant analysis
PCA	Principal component analysis
PLS-DA	Partial least squares discriminant analysis
VIP	Variable importance in projection
IHC	Immunohistochemistry
IF	Immunofluorescence
TME	Tumor microenvironment
PMN-MDSCs	Polymorphonuclear myeloid-derived suppressor cells
Tregs	Regulatory T cells
RNA-Seq	RNA sequencing
NLRs	NOD-like receptors
NK	Natural killer
FMN	Flavin mononucleotide
FAD	Flavin adenine dinucleotide
SD	Standard deviation

Acknowledgements

This work has been supported by Major Science and Technology Project of Qinghai Province (NO. 2021-SF-A4), Chinese Academy of Sciences - People's Government of Qinghai Province on Sanjiangyuan National Park (NO. LHZX-2022-01), and Qinghai Association for Science and Technology Youth and Middle-aged

Talent Support Program (NO. 2022QHSKXRCTJ35). We also acknowledge our colleagues for their work on this paper.

Clinical trial number

Not applicable.

Authors' contributions

Conceptualization: W.Z. Data curation: Y.L. Formal analysis: Y.L., Y.G., S.L., Y.M., and W.Z. Funding acquisition: L.W., and W.Z. Investigation: Y.L., Y.G., S.L., Y.M., Y.X., and W.Z. Methodology: Y.L. Resources: L.W. Supervision: L.W. Writing – original draft: Y.L., and W.Z. Writing – review & editing: L.W., and W.Z.

Funding

This work has been supported by Major Science and Technology Project of Qinghai Province (NO. 2021-SF-A4), Chinese Academy of Sciences - People's Government of Qinghai Province on Sanjiangyuan National Park (NO. LHZX-2022-01), and Qinghai Association for Science and Technology Youth and Middle-aged Talent Support Program (NO. 2022QHSKXRCTJ35).

Data availability

The datasets used and/or analyzed during the current study are available from the corresponding author upon reasonable request.

Declarations

Ethics approval and consent for publication

This study was approved by the Animal Experimentation Committee of Northwest Plateau Biology Institute, Chinese Academy of Sciences (allowance number NWIPB2023–19).

Consent for participation

Not applicable.

Competing interests

The authors declare no competing interests.

Author details

[1] Qinghai Provincial Key Laboratory of Tibetan Medicine Pharmacology and Safety Evaluation, Northwest Institute of Plateau Biology, Chinese Academy of Science, Xining 810008, China

[2] CAS Key Laboratory of Tibetan Medicine Research, Northwest Institute of Plateau Biology, Chinese Academy of Sciences, Xining 810001, China

[3] University of Chinese Academy of Sciences, Beijing, 100049, China

[4] College of Tibetan Medicine, Qinghai University, Xining 810016, China

References

1. Pan L, Wang X, Long F, Tang A. Clinical efficacy and safety

evaluation of traditional Chinese medicine for nourishing yin and replenishing qi in combination with PD-1/PD-L1 inhibitors in the treatment of NSCLC patients: a meta-analysis. Toxicol Res (Camb). 2025;14(1):tfaf013. https://doi.org/10.1093/toxres/tfaf013.

2. Li Y, Yan B, He S. Advances and challenges in the treatment of lung cancer. Biomed Pharmacother. 2023;169:115891. https://doi.org/10.1016/j.biopha.2023.115891.
3. Lv B, Wang Y, Ma D, Cheng W, Liu J, Yong T, et al. Immunotherapy: reshape the tumor immune microenvironment. Front Immunol. 2022;13:844142. https://doi.org/10.3389/fimmu.2022.844142.
4. Rui R, Zhou L, He S. Cancer immunotherapies: advances and bottlenecks. Front Immunol. 2023;14:1212476. https://doi.org/10.3389/fimmu.2023.1212476.
5. Shang S, Liu J, Verma V, Wu M, Welsh J, Yu J, et al. Combined treatment of non-small cell lung cancer using radiotherapy and immunotherapy: challenges and updates. Cancer Commun (Lond). 2021;41(11):1086-1099. https://doi.org/10.1002/cac2.12226.
6. Huang MY, Jiang XM, Wang BL, Sun Y, Lu JJ. Combination therapy with PD-1/PD-L1 blockade in non-small cell lung cancer: strategies and mechanisms. Pharmacol Ther. 2021;219:107694. https://doi.org/10.1016/j.pharmthera.2020.107694.
7. Lv J, Jia Y, Li J, Kuai W, Li Y, Guo F, Xu X, Zhao Z, Lv J, Li Z.

Gegen Qinlian decoction enhances the effect of PD-1 blockade in colorectal cancer with microsatellite stability by remodelling the gut microbiota and the tumour microenvironment. Cell Death Dis. 2019;10(6):415. https://doi.org/10.1038/s41419-019-1638-6.

8. Kong Q, Zhu H, Gong W, Deng X, Liu B, Dong J. Modified Bushen Yiqi formula enhances antitumor immunity by reducing the chemotactic recruitment of M2-TAMs and PMN-MDSCs in Lewis lung cancer-bearing mice. J Ethnopharmacol. 2024;319(Pt 1):117183. https://doi.org/10.1016/j.jep.2023.117183.
9. Li BB, Jiang YY, Li X, Yu MM, Meng Q, Wang DN, et al. Qingrehuoxue formula enhances anti-PD-1 immunotherapy in NSCLC by remodeling the tumor immune microenvironment via TREM2 signaling. BMC Complement Med Ther. 2025;25(1):270. https://doi.org/10.1186/s12906-025-05020-8.
10. Chen J, Li Y, Sun Q, Wang Y, Qiu Z, He X, et al. Huaier overcomes tumor-induced immunosuppression in colorectal cancer by activating MHC I and CD8+ T cells. Phytomedicine. 2025;147:157157. https://doi.org/10.1016/j.phymed.2025.157157.
11. Zhou WB, Liu YY, Gao YQ, Suonanlamao, Ma YA, Xiao YC, et al. Integrating proteomics, metabolomics, and network pharmacology to investigate the mechanism of *Cordyceps sinensis* in the treatment of COPD rats. J Pharm Biomed Anal. 2025;266:117076. https://doi.org/10.1016/j.jpba.2025.117076.
12. Li CX, Yang S, Qiu SJ, Lian YB, Qiu YN. Study on the efficacy of

Bailing capsule on chemotherapy-associated fatigue in lung cancer. Chin. & For. Med. Res. 2016;14(20):51-52. https://doi.org/10.14033/j.cnki.cfmr.2016.20.026.

13. Guo J. Observation on the therapeutic effect of Jiawei Lifting and Dispersing combined with Bailing Capsule in the treatment of chemotherapy complications of lung cancer. Shaanxi J. Tradit. Chin. Med. 2017;38(6):699-700. https://doi.org/10.3969/j.issn.10.3969/j.issn.1000-7369.2017.06.008.
14. Tang L. Regulatory effect of Yupingfeng granules combined with Bailing capsule on immune function of lung cancer chemotherapy patients. Mod. J. Integr. Tradit. Chin. West. Med. 2015;24(12):1318-1319. https://doi.org/10.3969/j.issn.1008-8849.2015.12.024.
15. Wang C, Wang J, Qi Y. Adjuvant treatment with *Cordyceps sinensis* for lung cancer: A systematic review and meta-analysis of randomized controlled trials. J Ethnopharmacol. 2024;327:118044. https://doi.org/10.1016/j.jep.2024.118044.
16. Lu T, Zhou L, Chu Z, Song Y, Wang Q, Zhao M, et al. *Cordyceps sinensis* relieves non-small cell lung cancer by inhibiting the MAPK pathway. Chin Med. 2024;19(1):54. https://doi.org/10.1186/s13020-024-00895-0.
17. Zhou J, Hou D, Zou W, Wang J, Luo R, Wang M, et al. Comparison of Widely Targeted Metabolomics and Untargeted Metabolomics of Wild *Ophiocordyceps sinensis*. Molecules. 2022;27(11):3645. https://doi.org/10.3390/molecules27113645.

18. Liu YY, Dou GJ, Xiao YC, Chen XY, Wei LX, Zhou WB. Therapeutic potential of *Cordyceps sinensis* targeting oxidative stress and inflammatory response in the treatment of COPD rats: insights from metabolomics analysis. J Asian Nat Prod Res. 2025;27(3):460-477. https://doi.org/10.1080/10286020.2024.2403611.
19. Koh CH, Lee S, Kwak M, Kim BS, Chung Y. CD8 T-cell subsets: heterogeneity, functions, and therapeutic potential. Exp Mol Med. 2023;55(11):2287-2299. https://doi.org/10.1038/s12276-023-01105-x.
20. Huang Z, Li B, Guo Y, Wu L, Kou F, Yang L. Signatures of multi-omics reveal distinct tumor immune microenvironment contributing to immunotherapy in lung adenocarcinoma. Front Immunol. 2021;12:723172. https://doi.org/10.3389/fimmu.2021.723172.
21. Fu L, Deng R, Huang Y, Yang X, Jiang N, Zhou J, et al. DGKA interacts with SRC/FAK to promote the metastasis of non-small cell lung cancer. Cancer Lett. 2022;532:215585. https://doi.org/10.1016/j.canlet.2022.215585.
22. Peng D, Yang W, Tang T, He A, Xu X, Jing T, et al. PLA2G7 promotes immune evasion of bladder cancer through the JAK-STAT-PDL1 axis. Cell Death Dis. 2025;16(1):234. https://doi.org/10.1038/s41419-025-07593-1.
23. Zhang F, Liu W, Meng F, Jiang Q, Tang W, Liu Z, et al. Inhibiting PLA2G7 reverses the immunosuppressive function of

intratumoral macrophages and augments immunotherapy response in hepatocellular carcinoma. J Immunother Cancer. 2024;12(1):e008094. https://doi.org/10.1136/jitc-2023-008094.

24. Wang G, Qiu M, Xing X, Zhou J, Yao H, Li M, et al. Lung cancer scRNA-seq and lipidomics reveal aberrant lipid metabolism for early-stage diagnosis. Sci Transl Med. 2022;14(630):eabk2756. https://doi.org/10.1126/scitranslmed.abk2756.
25. Jiang X, Fan Z, Zhang Z, Zeng F, Sun T, Li Y, et al. Tumor metabolome remolded by low dose mitochondrial uncoupler elicites robust $CD8^+$ T cell response. Cell Death Discov. 2025;11(1):291. https://doi.org/10.1038/s41420-025-02584-9.
26. Lan Y, Du W, Ma Y, Cao J. Prognostic value and immune infiltration of novel markers TNRC6C/AMPD1 in pancreatic cancer microenvironment. Biochem Biophys Rep. 2025;43:102185. https://doi.org/10.1016/j.bbrep.2025.102185.
27. Yang L, Liu Y, Zhang B, Yu M, Huang F, Wen Y, et al. Prognostic tumor microenvironment gene and the relationship with immune infiltration characteristics in metastatic breast cancer. BIOCELL. 2022;46(5):1215-1243. https://doi.org/10.32604/biocell.2022.018221.
28. Yang L, Li A, Yu W, Wang H, Zhang L, Wang D, et al. Blockade of purine metabolism reverses macrophage immunosuppression and enhances anti-tumor immunity in non-small cell lung cancer. Drug Resist Updat. 2025;78:101175. https://doi.org/10.1016/j.drup.2024.101175.

29. Wo YJ, Gan ASP, Lim X, Tay ISY, Lim S, Lim JCT, et al. The Roles of CD38 and CD157 in the Solid Tumor Microenvironment and Cancer Immunotherapy. Cells. 2019;9(1):26. https://doi.org/10.3390/cells9010026.
30. Ortolan E, Augeri S, Fissolo G, Musso I, Funaro A. CD157: From immunoregulatory protein to potential therapeutic target. Immunol Lett. 2019;205:59-64. https://doi.org/10.1016/j.imlet.2018.06.007.
31. Agliano F, Karginov TA, M é noret A, Provatas A, Vella AT. Nicotinamide breaks effector CD8 T cell responses by targeting mTOR signaling. iScience. 2022;25(3):103932. https://doi.org/10.1016/j.isci.2022.103932.

Figure Captions

Fig. 1 Inhibitory effects of *C. sinensis* and anti-mouse PD-1 on tumors in mice with LLC (n = 8). (**A**) Means of body weight change among the eight groups. (**B**) Tumor volume among the eight groups. (**C**) Tumor weight among the eight groups. (**D-K**) The H&E staining of tumor tissues in the eight groups (magnification, 200×). D: Vehicle, E: mPD-1, F: L-CS, G: M-CS, H: H-CS, I: L-CS + mPD-1, J: M-CS + mPD-1, K: H-CS + mPD-1. $^{*}P < 0.05$, $^{**}P < 0.01$ *vs.* the Vehicle group, $^{\#\#}P < 0.01$ *vs.* the mPD-1 group, $^{\$}P < 0.05$ *vs.* the M-CS group. Black arrows indicate mitotic figures, yellow arrows indicate patchy necrosis of the tumor cells, green arrows indicate extensive hemorrhage, and blue arrows indicate the cytoplasm of the neoplastic cells exhibits a loosely arranged pattern.

Fig. 2 Effects of *C. sinensis* and anti-mouse PD-1 on immune cell infiltration in the blood of mice with LLC (n = 8). (**A**) Proportion of $CD45^+$ cells. (**B**) Proportion of $CD3^+$ T cells. (**C**) Proportion of $CD8^+$ T cells and $CD4^+$ T cells. (**D**) Proportion of $Foxp3^+$ Tregs. (**E**) The bar chart displays the proportions of $CD45^+$ cells, $CD3^+$ T cells, $CD8^+$ T cells, $CD4^+$ T cells, and $Foxp3^+$ Tregs. $^{*}P < 0.05$, $^{**}P < 0.01$ *vs.* the Vehicle group, $^{\#\#}P < 0.01$ *vs.* the mPD-1 group, $^{\$}P < 0.05$, $^{\$\$}P < 0.01$ *vs.* the M-CS group.

Fig. 3 Effects of *C. sinensis* and anti-mouse PD-1 on immune cell infiltration in the tumors of mice with LLC (n = 8). (**A**) IHC staining of $CD3^+$ T cells. (**B**) IHC staining of $CD8^+$ T cells. (**C**) IHC staining of $CD4^+$ T cells. (**D**) IHC staining of $Foxp3^+$ Tregs. (**E**) IF staining of

$CD11b^+Ly6G^+$ cells. (**F**) IHC scores of $CD3^+/CD45^+$, $CD8^+/CD3^+$, $CD4^+/CD3^+$, $Foxp3^+/CD4^+$ cells, and IF score of $CD11b^+Ly6G^+$ cells. $^*P < 0.05$, $^{**}P < 0.01$ *vs.* the Vehicle group, $^{\#}P < 0.05$, $^{\#\#}P < 0.01$ *vs.* the mPD-1 group, $^{\$\$}P < 0.01$ *vs.* the M-CS group.

Fig. 4 RNA-seq analysis of TME modulation by *C. sinensis* and anti-mouse PD-1 in mice with LLC (n = 6). (**A-C**) Volcano plots of differential genes. A: mPD-1 *vs.* Vehicle group, B: M-CS *vs.* Vehicle group, C: M-CS + mPD-1 *vs.* Vehicle group. (**D**) Top 20 KEGG pathways enriched in the mPD-1 group compared to the Vehicle group. (**E**) Top 20 KEGG pathways enriched in the M-CS group compared to the Vehicle group. (**F**) Top 20 KEGG pathways enriched in the M-CS + mPD-1 group compared to the Vehicle group. (**G**) Heatmap of DEGs among the Vehicle, mPD-1, M-CS, and M-CS + mPD-1 groups. (**H**) Heatmap of immune cell infiltration assessed by the MCP counter algorithm. (**I**) Immune cell fractions were determined using CIBERSORT (n = 3). (**J**) GSEA plot for $CD8^+$ T cells activation based on DEGs between the M-CS + mPD-1 and Vehicle groups. (**K**) GSEA plot for $CD4^+$ T cells activation based on DEGs between the M-CS + mPD-1 and Vehicle groups. (**L**) GSEA plot for Treg cells activation based on DEGs between the M-CS + mPD-1 and Vehicle groups. $^*P < 0.05$, $^{**}P < 0.01$ *vs.* the Vehicle group.

Fig. 5 Metabolomics analysis of the tumor in mice with LLC treated with *C. sinensis* and anti-mouse PD-1 (n = 6). (**A-C**) Score plots for the PCA, PLS-DA, and OPLS-DA analyses of metabolic data from the Vehicle, mPD-1, M-CS, and M-CS + mPD-1 groups in positive and

negative ion modes, respectively. (**D, G, J**) Score plots for the OPLS-DA analysis of metabolic data from the Vehicle, mPD-1, M-CS, and M-CS + mPD-1 groups. (**E, H, K**) Permutation tests of the OPLS-DA analysis. (**F, I, L**) Volcano plots of differential metabolites. (**M-O**) Pathway enrichment analysis of differentially expressed metabolites in the mPD-1, M-CS, and M-CS + mPD-1 groups compared with the Vehicle group.

Fig. 6 The combination of *C. sinensis* and anti-mouse PD-1 induced specific changes in the metabolome. (**A**) Venn diagram of differentially expressed metabolites from the Vehicle, mPD-1, M-CS, and M-CS + mPD-1 groups. (**B**) Pathway enrichment analysis of 124 specific metabolites in the M-CS + mPD-1 group compared to the Vehicle group. (**C**) Heatmap showing normalized relative abundances of metabolites, with annotation, that were significantly changed in the M-CS + mPD-1 group compared to the Vehicle group and in the mPD-1 group compared to the Vehicle group, but not in the M-CS group compared to the Vehicle group.

Fig. 7 Compound-reaction-enzyme-gene network. (**A**) Glycerophospholipid metabolism, the TCA cycle, purine metabolism and nicotinate and nicotinamide metabolism. (**B**) Expression levels of the associated genes in the Vehicle and M-CS + mPD-1 groups. Metabolites (hexagons), genes (circles), metabolic enzymes (squares), and reactions (diamonds) are presented as nodes. Input genes are shown in blue, input metabolites are shown in red. $^{*}P < 0.05$, $^{**}P < 0.01$ *vs.* the Vehicle group.

Fig. 8 Potential mechanism of the combination of *C. sinensis* and anti-mouse PD-1 therapy in mice with LLC.

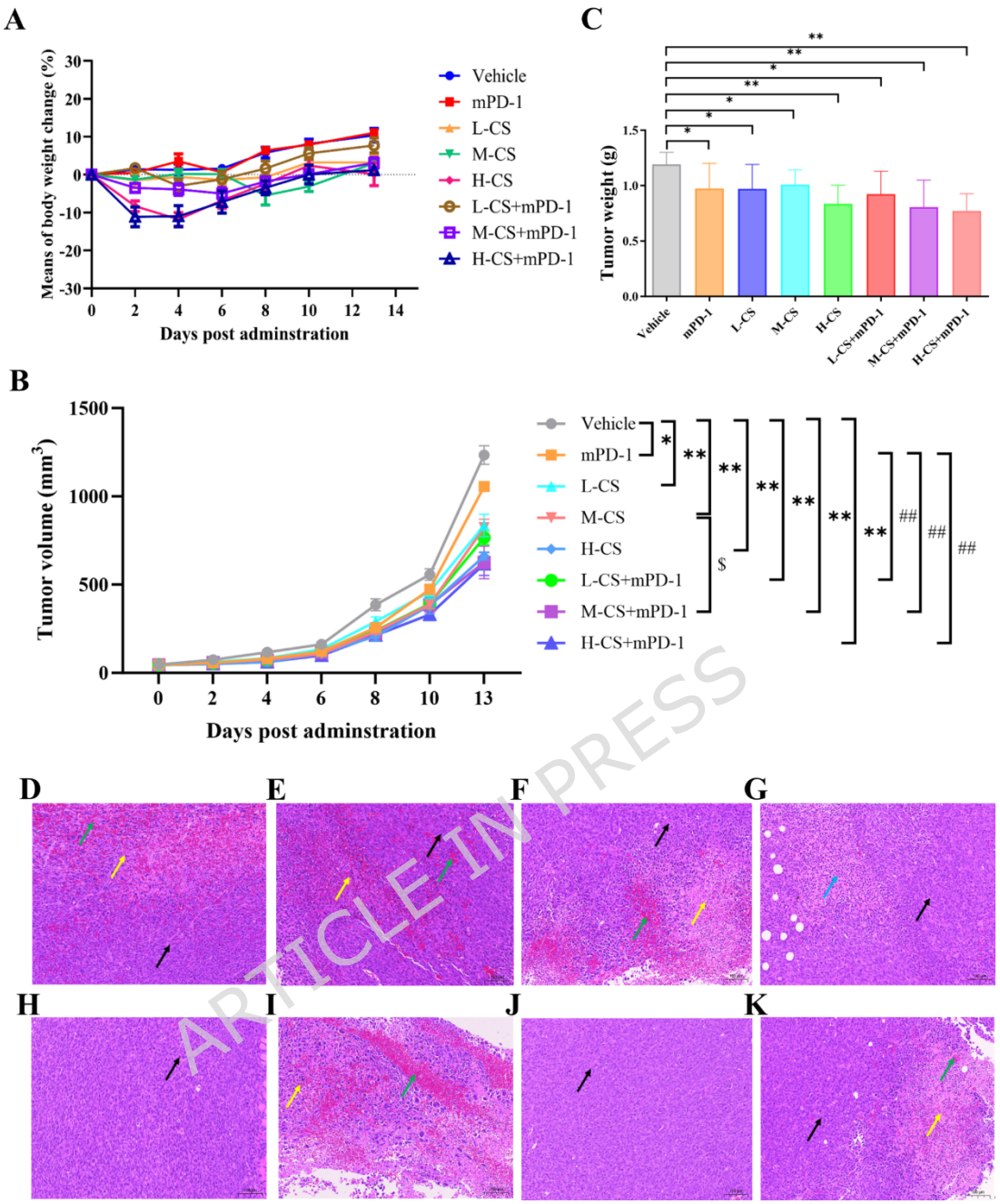

Fig. 1 Inhibitory effects of *C. sinensis* and anti-mouse PD-1 on tumors in mice with LLC (n = 8). (**A**) Means of body weight change among the eight groups. (**B**) Tumor volume among the eight groups. (**C**) Tumor weight among the eight groups. (**D-K**) The H&E staining of tumor tissues in the eight groups (magnification, 200×). D: Vehicle, E: mPD-1, F: L-CS, G: M-CS, H: H-CS, I: L-CS + mPD-1, J: M-CS + mPD-1, K: H-CS + mPD-1. $^{*}P < 0.05$, $^{**}P < 0.01$ *vs.* the Vehicle group, $^{\#\#}P < 0.01$ *vs.* the mPD-1 group, $^{\$}P < 0.05$ *vs.* the M-CS group. Black arrows indicate mitotic figures, yellow arrows indicate patchy necrosis of the tumor cells, green arrows indicate extensive hemorrhage, and blue arrows indicate the cytoplasm of the neoplastic cells exhibits a loosely arranged pattern.

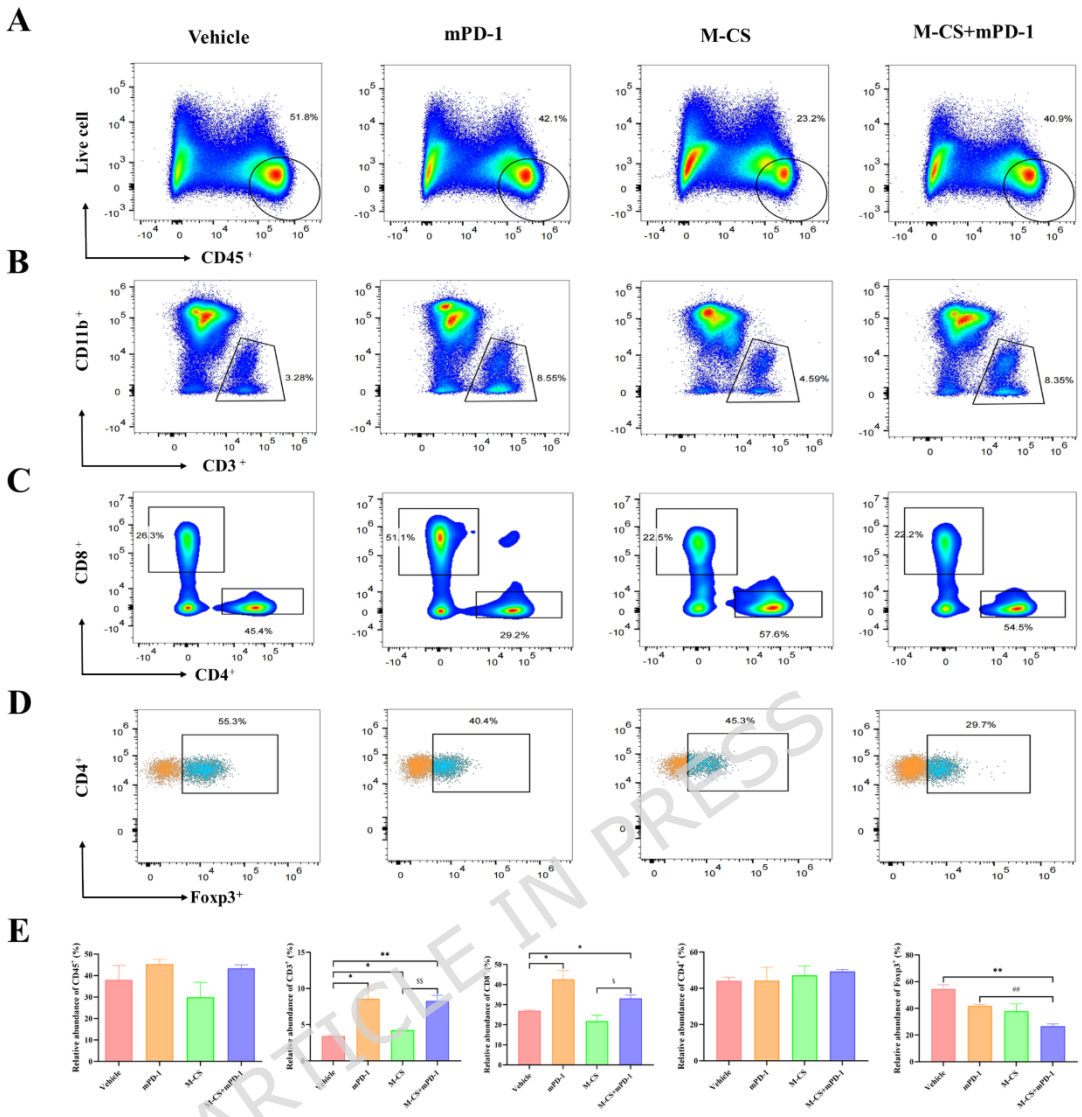

Fig. 2 Effects of *C. sinensis* and anti-mouse PD-1 on immune cell infiltration in the blood of mice with LLC (n = 8). (**A**) Proportion of CD45$^+$ cells. (**B**) Proportion of CD3$^+$ T cells. (**C**) Proportion of CD8$^+$ T cells and CD4$^+$ T cells. (**D**) Proportion of Foxp3$^+$ Tregs. (**E**) The bar chart displays the proportions of CD45$^+$ cells, CD3$^+$ T cells, CD8$^+$ T cells, CD4$^+$ T cells, and Foxp3$^+$ Tregs. $^*P < 0.05$, $^{**}P < 0.01$ *vs.* the Vehicle group, $^{\#\#}P < 0.01$ *vs.* the mPD-1 group, $^{\$}P < 0.05$, $^{\$\$}P < 0.01$ *vs.* the M-CS group.

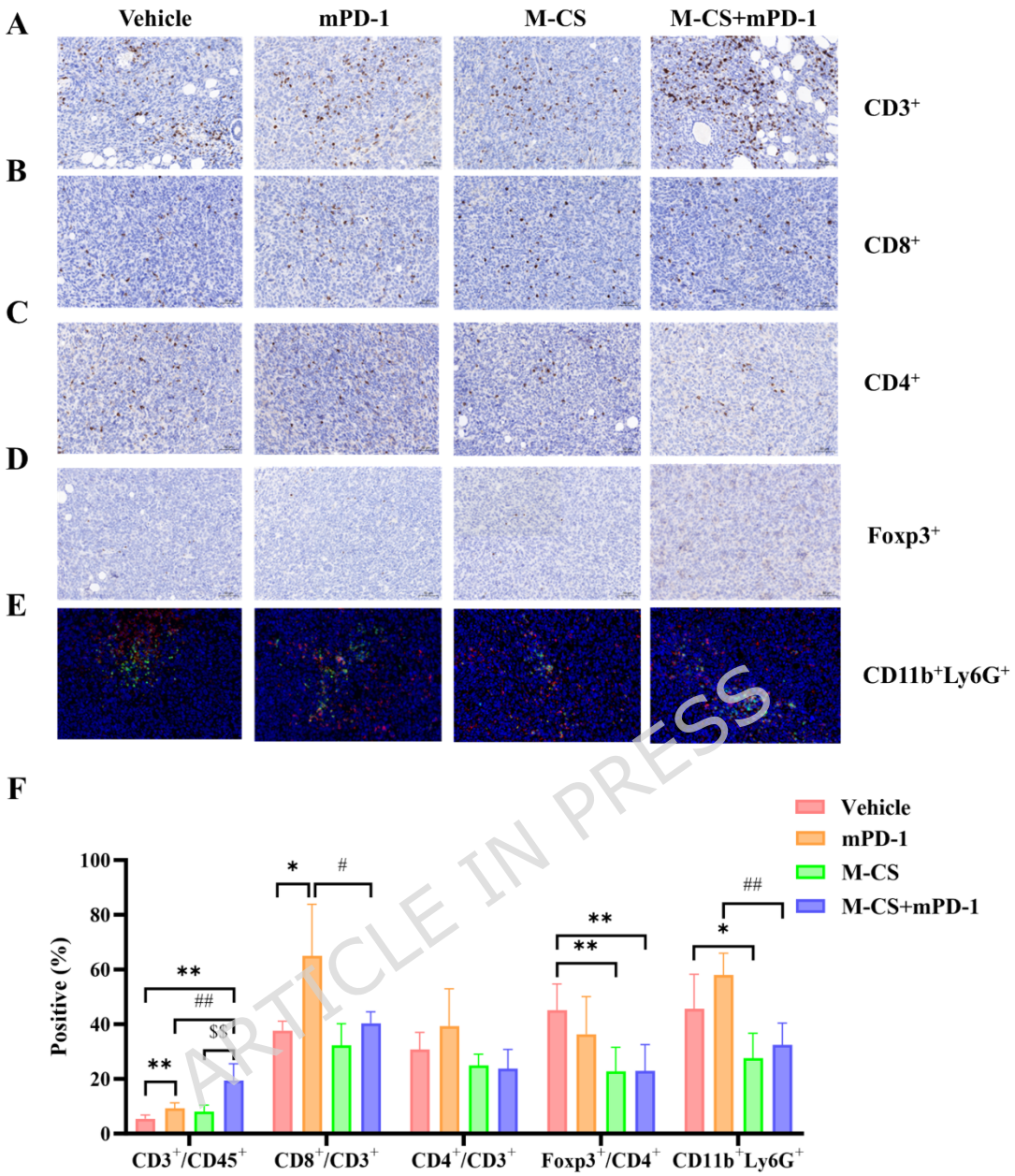

Fig. 3 Effects of *C. sinensis* and anti-mouse PD-1 on immune cell infiltration in the tumors of mice with LLC (n = 8). (**A**) IHC staining of $CD3^+$ T cells. (**B**) IHC staining of $CD8^+$ T cells. (**C**) IHC staining of $CD4^+$ T cells. (**D**) IHC staining of $Foxp3^+$ Tregs. (**E**) IF staining of $CD11b^+Ly6G^+$ cells. (**F**) IHC scores of $CD3^+/CD45^+$, $CD8^+/CD3^+$, $CD4^+/CD3^+$, $Foxp3^+/CD4^+$ cells, and IF score of $CD11b^+Ly6G^+$ cells. $^*P < 0.05$, $^{**}P < 0.01$ *vs.* the Vehicle group, $^{\#}P < 0.05$, $^{\#\#}P < 0.01$ *vs.* the mPD-1 group, $^{\$\$}P < 0.01$ *vs.* the M-CS group.

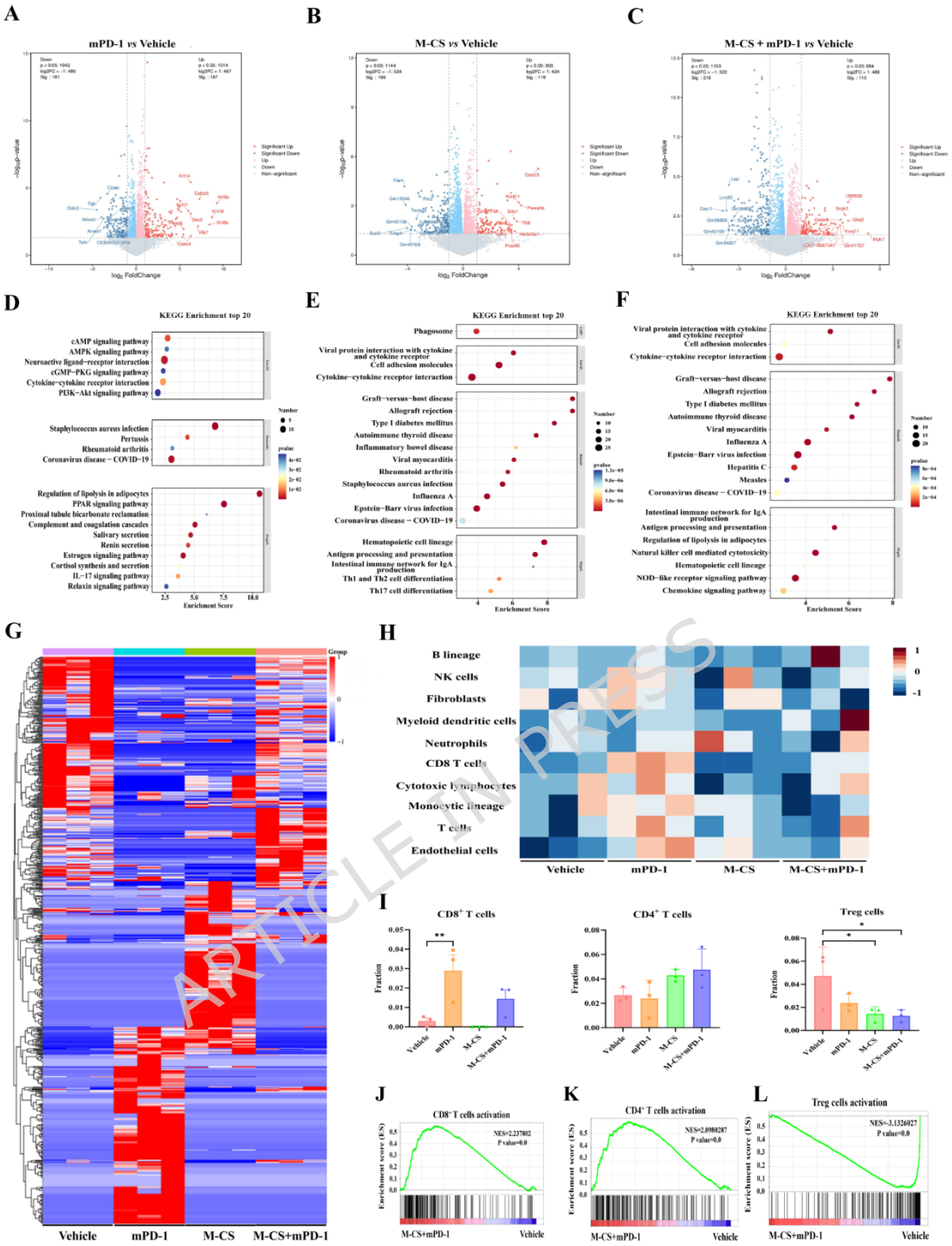

Fig. 4 RNA-seq analysis of TME modulation by *C. sinensis* and anti-mouse PD-1 in mice with LLC (n = 6). (**A-C**) Volcano plots of differential genes. A: mPD-1 *vs.* Vehicle group, B: M-CS *vs.* Vehicle group, C: M-CS + mPD-1 *vs.* Vehicle group. (**D**) Top 20 KEGG pathways enriched in the mPD-1 group compared to the Vehicle group. (**E**) Top 20 KEGG pathways enriched in the M-CS group compared to the Vehicle group. (**F**) Top 20 KEGG pathways enriched in the M-CS + mPD-1 group compared to the Vehicle group. (**G**) Heatmap of DEGs among the Vehicle, mPD-1, M-CS, and M-CS + mPD-1 groups. (**H**) Heatmap of immune cell infiltration assessed by

the MCP counter algorithm. (**I**) Immune cell fractions were determined using CIBERSORT (n = 3). (**J**) GSEA plot for $CD8^+$ T cells activation based on DEGs between the M-CS + mPD-1 and Vehicle groups. (**K**) GSEA plot for $CD4^+$ T cells activation based on DEGs between the M-CS + mPD-1 and Vehicle groups. (**L**) GSEA plot for Treg cells activation based on DEGs between the M-CS + mPD-1 and Vehicle groups. $^{*}P < 0.05$, $^{**}P < 0.01$ *vs.* the Vehicle group.

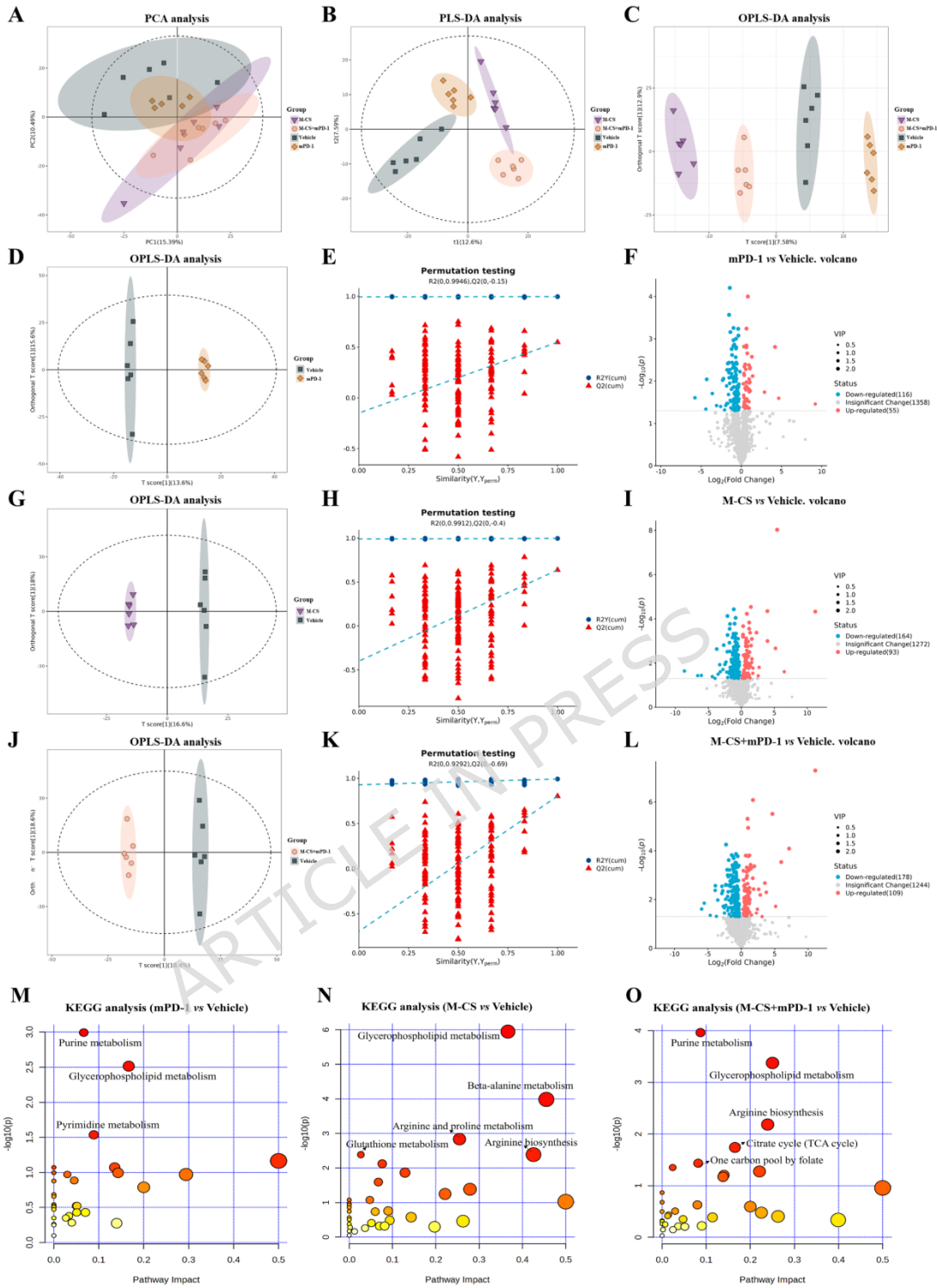

Fig. 5 Metabolomics analysis of the tumor in mice with LLC treated with *C. sinensis* and anti-mouse PD-1 (n = 6). (**A-C**) Score plots for the PCA, PLS-DA, and OPLS-DA analyses of metabolic data from the Vehicle, mPD-1, M-CS, and M-CS + mPD-1 groups in positive and negative ion modes, respectively. (**D, G, J**) Score plots for the OPLS-DA analysis of metabolic data from the Vehicle, mPD-1, M-CS, and M-CS + mPD-1 groups. (**E, H, K**) Permutation tests of the OPLS-DA

analysis. (**F, I, L**) Volcano plots of differential metabolites. (**M-O**) Pathway enrichment analysis of differentially expressed metabolites in the mPD-1, M-CS, and M-CS + mPD-1 groups compared with the Vehicle group.

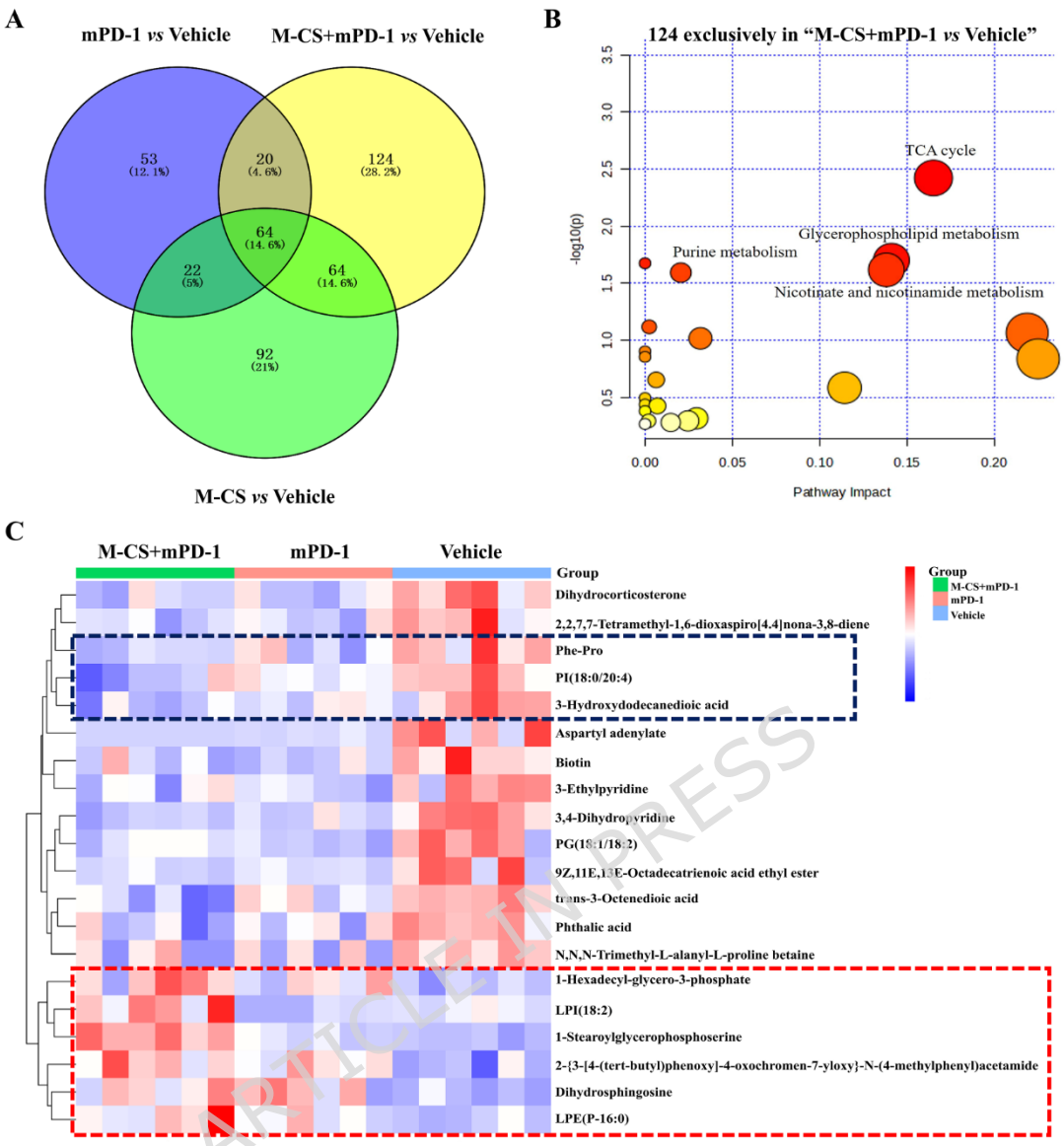

Fig. 6 The combination of *C. sinensis* and anti-mouse PD-1 induced specific changes in the metabolome. (**A**) Venn diagram of differentially expressed metabolites from the Vehicle, mPD-1, M-CS, and M-CS + mPD-1 groups. (**B**) Pathway enrichment analysis of 124 specific metabolites in the M-CS + mPD-1 group compared to the Vehicle group. (**C**) Heatmap showing normalized relative abundances of metabolites, with annotation, that were significantly changed in the M-CS + mPD-1 group compared to the Vehicle group and in the mPD-1 group compared to the Vehicle group, but not in the M-CS group compared to the Vehicle group.

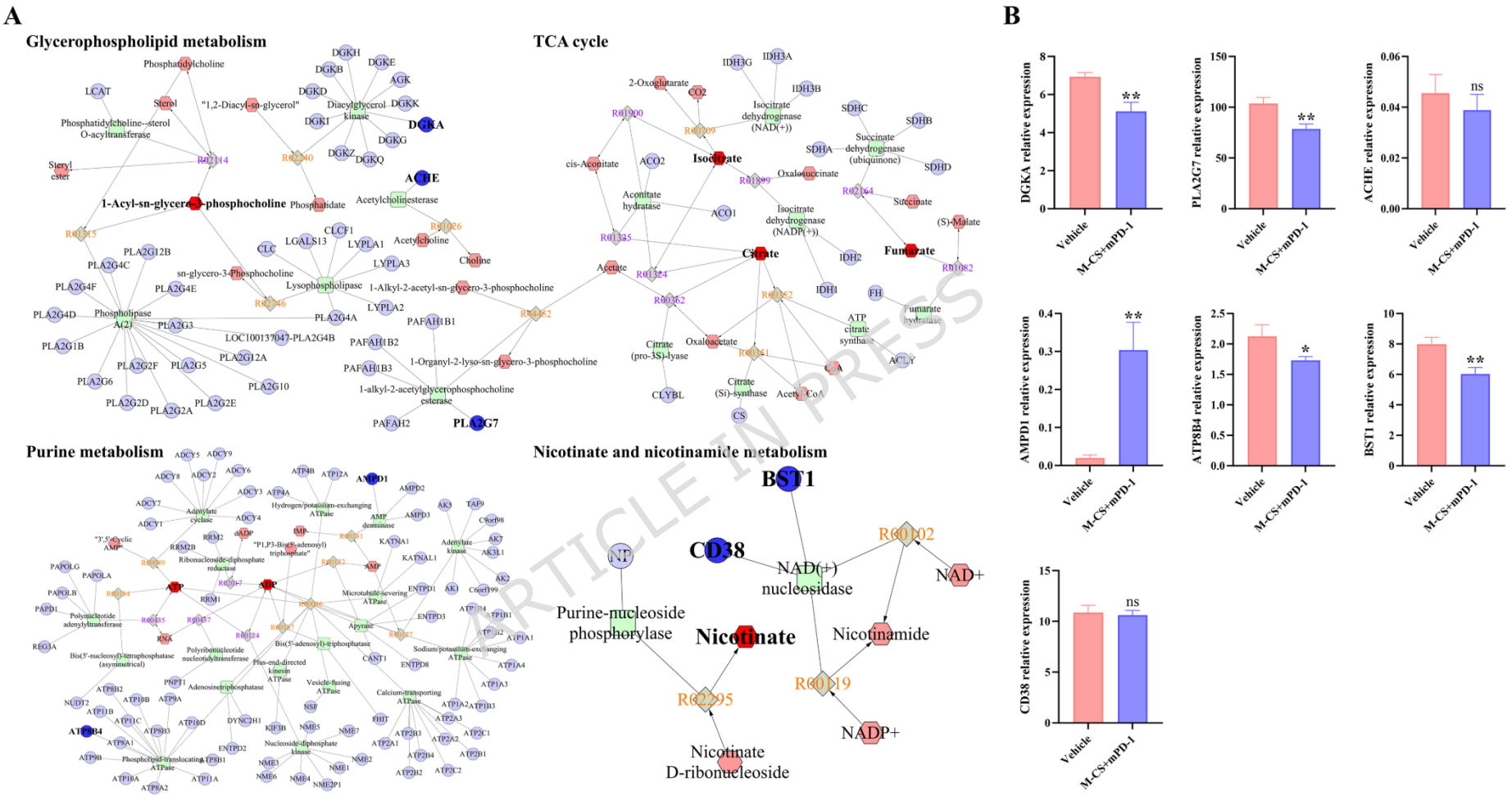

Fig. 7 Compound-reaction-enzyme-gene network. (**A**) Glycerophospholipid metabolism, the TCA cycle, purine metabolism and nicotinate and nicotinamide metabolism. (**B**) Expression levels of the associated genes in the

Vehicle and M-CS + mPD-1 groups. Metabolites (hexagons), genes (circles), metabolic enzymes (squares), and reactions (diamonds) are presented as nodes. Input genes are shown in blue, input metabolites are shown in red. $^{*}P < 0.05$, $^{**}P < 0.01$ *vs.* the Vehicle group.

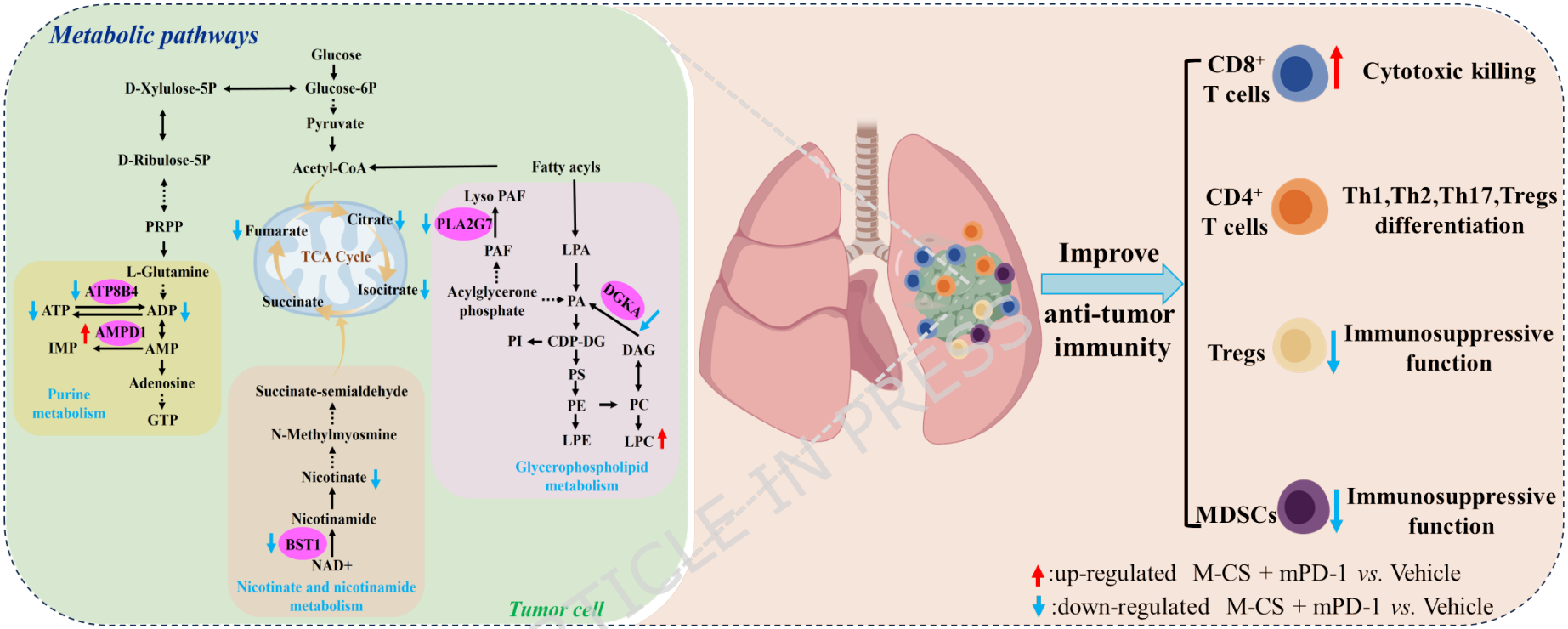

Fig. 8 Potential mechanism of the combination of *C. sinensis* and anti-mouse PD-1 therapy in mice with LLC.

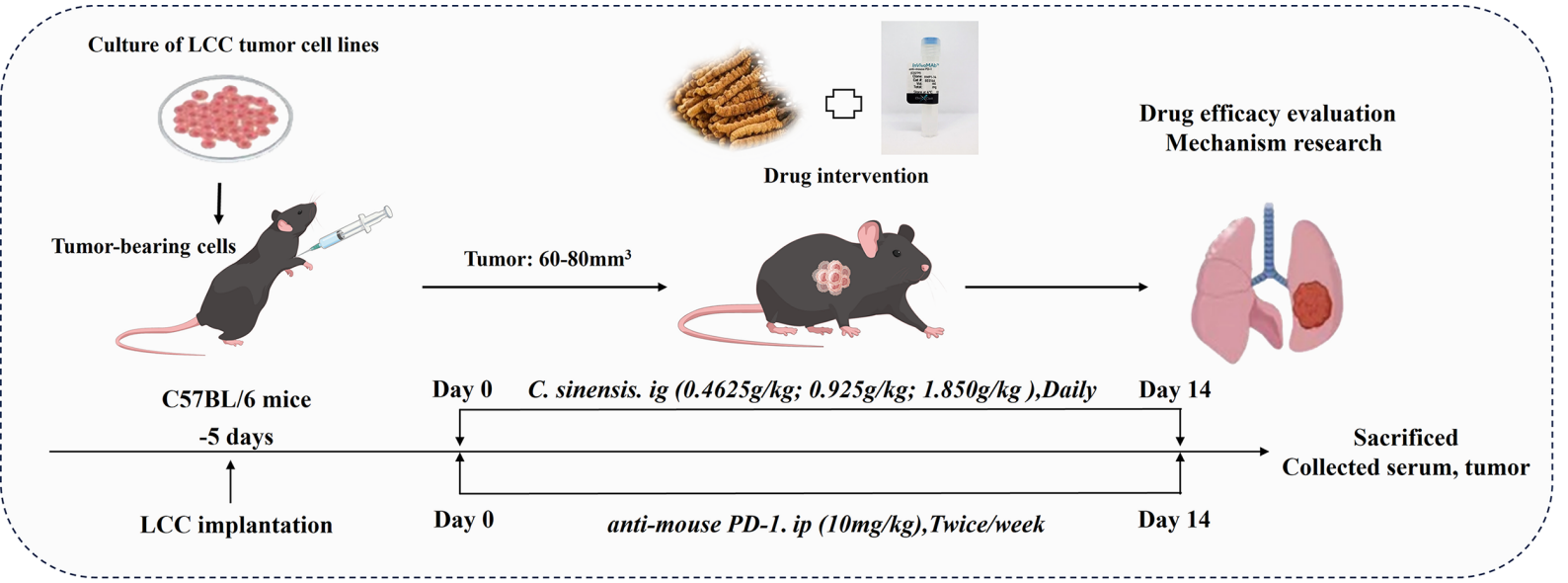
Culture of LCC tumor cell lines
Tumor-bearing cells
C57BL/6 mice
-5 days
LCC implantation
Tumor: 60-80mm3
Drug intervention
Drug efficacy evaluation
Mechanism research
Day 0
C. sinensis. ig (0.4625g/kg; 0.925g/kg; 1.850g/kg),Daily
Day 14
Sacrificed
Collected serum, tumor
Day 0
anti-mouse PD-1. ip (10mg/kg),Twice/week
Day 14

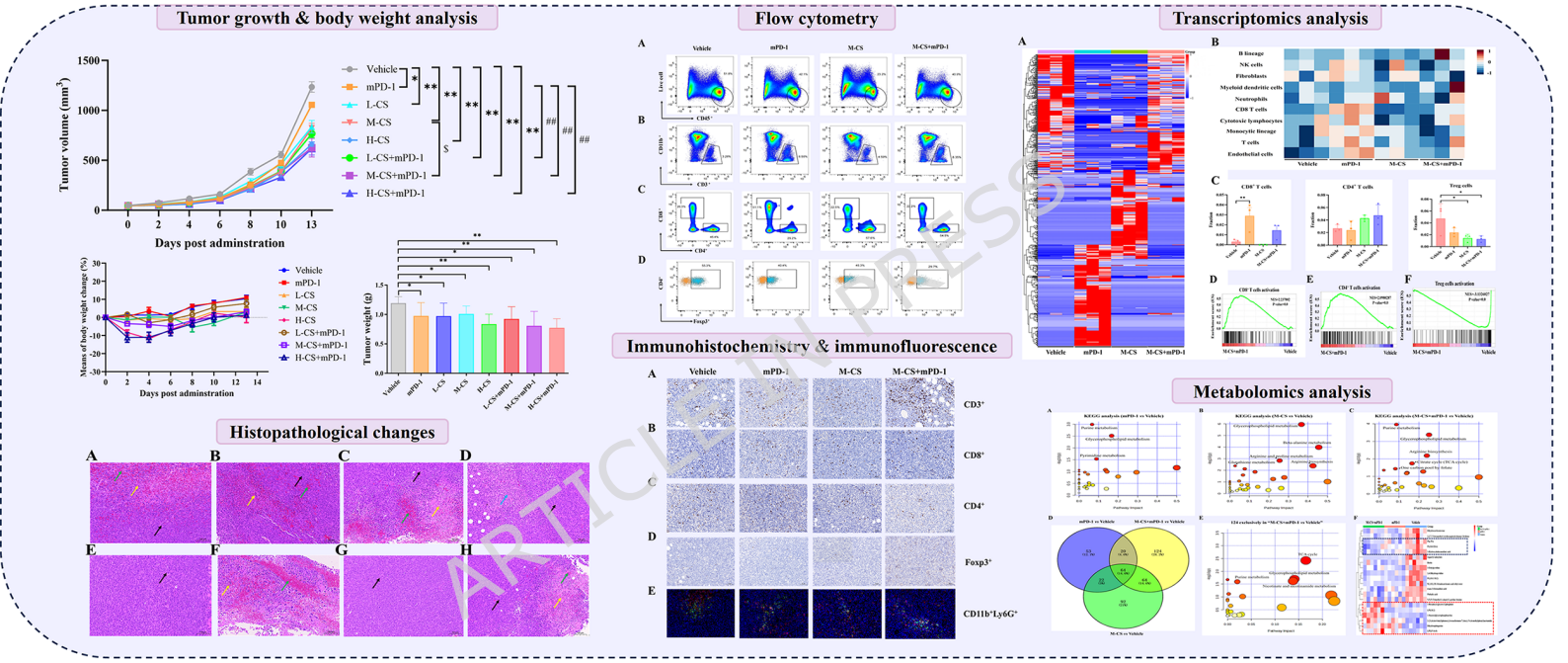
Tumor growth & body weight analysis
Tumor volume (mm3)
Days post adminstration
Vehicle
mPD-1
L-CS
M-CS
H-CS
L-CS+mPD-1
M-CS+mPD-1
H-CS+mPD-1
Mean of body weight change (%)
Tumor weight (g)
Flow cytometry
Immunohistochemistry & immunofluorescence
CD3+
CD8+
CD4+
Foxp3+
CD11b+Ly6G+
Histopathological changes
Transcriptomics analysis
Metabolomics analysis

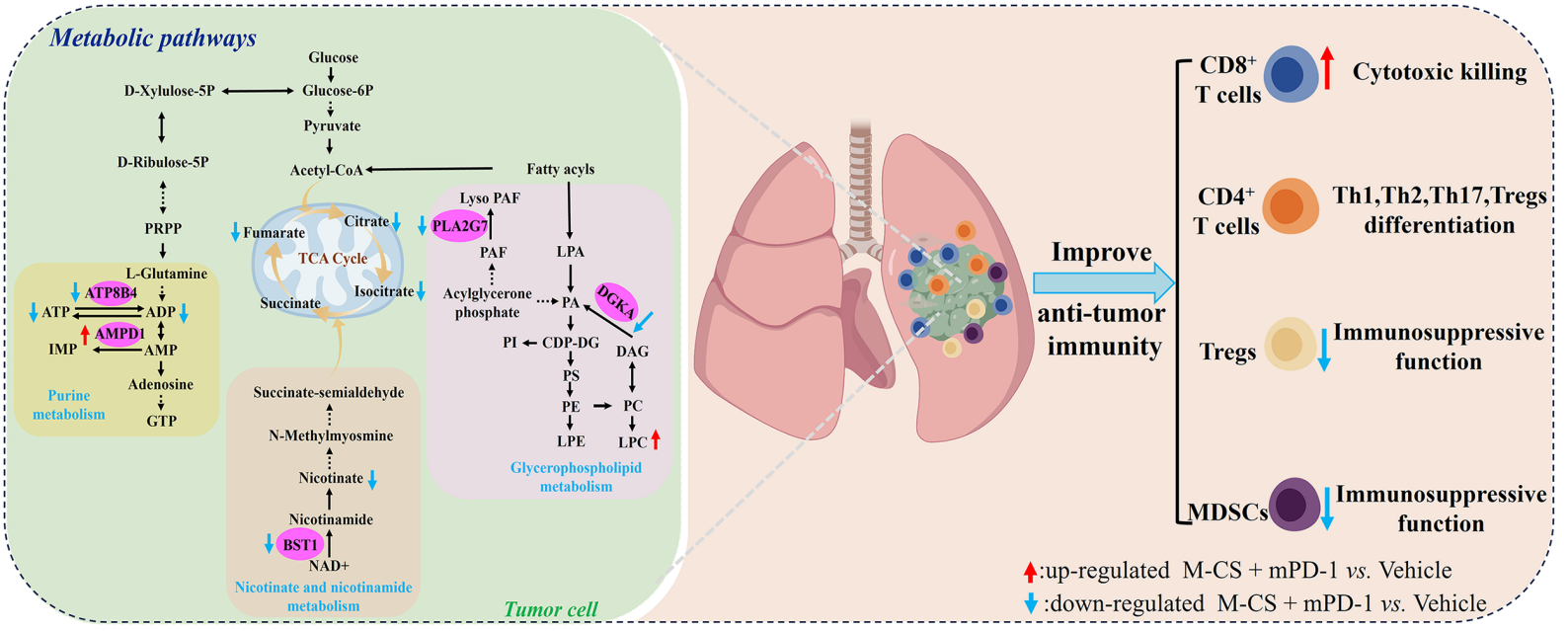
Metabolic pathways
Glucose
D-Xylulose-5P
Glucose-6P
Pyruvate
D-Ribulose-5P
Acetyl-CoA
Fatty acyls
PRPP
L-Glutamine
ATP8B4
ATP
ADP
AMPD1
IMP
AMP
Adenosine
GTP
Purine metabolism
Fumarate
Citrate
TCA Cycle
Succinate
Isocitrate
Lyso PAF
PLA2G7
PAF
LPA
Acylglycerone phosphate
PA
DGKA
PI
CDP-DG
DAG
PS
PE
PC
LPE
LPC
Glycerophospholipid metabolism
Succinate-semialdehyde
N-Methylmyosmine
Nicotinate
Nicotinamide
BST1
NAD+
Nicotinate and nicotinamide metabolism
Tumor cell
Improve
anti-tumor
immunity
CD8+ T cells
Cytotoxic killing
CD4+ T cells
Th1,Th2,Th17,Tregs differentiation
Tregs
Immunosuppressive function
MDSCs
Immunosuppressive function
:up-regulated M-CS + mPD-1 vs. Vehicle
:down-regulated M-CS + mPD-1 vs. Vehicle